Electrochimica Acta 55 (2010) 2139–2148

Contents lists available at ScienceDirect

Electrochimica Acta

journal homepage: www.elsevier.com/locate/electacta

Nanoflakes of the cobaltous oxide, CoO: Synthesis and characterization

H. Heli[a,*], H. Yadegari[b]

[a] *Department of Chemistry, Islamic Azad University, Fars Science and Research Branch, P.O. Box: 73715-181, Marvdasht, Iran*
[b] *Department of Chemistry, K.N. Toosi University of Technology, Tehran, Iran*

ARTICLE INFO

Article history:
Received 9 October 2009
Received in revised form
10 November 2009
Accepted 15 November 2009
Available online 21 December 2009

Keywords:
Cobaltous oxide
Nanoflake
AFM
STM
Impedance spectroscopy

ABSTRACT

Nanoflakes of the cobaltous oxide as a thin film were deposited from a 100 mM cobalt (II) nitrate solution potentiostatically at −1000 mV (vs. Ag/AgCl) onto a platinum electrode surface. Surface morphology of the cobaltous oxide was studied by surface microscopy techniques (SEM, AFM and STM) and the electrochemical behavior was evaluated in alkaline solution using cyclic voltammetry and electrochemical impedance spectroscopy. Using cyclic voltammetry, the electron-transfer coefficient and the apparent charge-transfer rate constant of various redox transitions were determined. The cobaltous oxide electrode represented prominent electrocatalytic activity toward the mediated electrooxidation of ascorbic acid, glucose and methanol. In the Nyquist diagrams, different time constants appeared with relation to different physicochemical processes.

1. Introduction

Metal and metal oxide nanostructured have become an area of growing interest and importance in a wide range of fundamental studies and technological applications, due to their unique size- and shape-dependent activities, optical, electronic, magnetic, chemical, electrochemical and mechanical properties when compared to their bulk counterparts [1]. These nanostructured materials represent comparable characteristic length scales with the critical length scales of physical phenomena [2], quantum confinement phenomena [3] and surface effects [4] which lead to size- and shape-dependent kinetics and thermodynamics [5]. Herein, nanostructured oxide materials have played important roles in corrosion, catalysis, electrocatalysis, electroanalysis, fuel cells, and photonic processes [5–8].

The preparation and characterization of cobalt oxides have been extensively studied due to attractive applications in batteries [9], supercapacitors [10], solar cells [11], catalysis [12], corrosion protective coatings [13], magnetic nanostructures and magnetic storage systems [14], electrochromic [15] and other devices [16]. Cobalt oxides have also been used in oxygen evolution [17] and reduction [18] reactions, ion exchange process [19] and design of the modified electrodes aiming at applications in electrooxidation of carbohydrates and thiols [20–22], hydrogen peroxide [23], aspirin and acetaminophen [24], hydroquinone [25] and alcohols [26]. In this regard, various methods of preparation, ranging from spray pyrolysis [27], sonication assisted methods [28], sputtering [29], thermal salt decomposition [30], powder immobilization [31], γ-irradiation [32], sol–gel technique [33] to electrodeposition from aqueous solutions [12,20,21,24,34] have been considered. Among the approached methods mentioned above, those which attained to nanostructured cobalt oxides are of the most interesting. This is due to the superior physical and chemical properties of nanosize of this oxide, compared to the polycrystalline counterpart [35]. Superior characteristics of nanostructured cobalt oxides can arise from the enhancement of surface reactivity upon particle size decreasing [36], presence of high degree of defects and disorders at the surface [37] and nonstoichiometric phase [38], unique electronic structures and higher activities for solid-state ion transport [39]. Nanostructured cobalt oxides were synthesized using different methods of mechanochemical synthesis [40], reduction/oxidation route [32] metal organic chemical vapor deposition [41], and chemical precipitation in the presence of poly(ethyleneimine) as a soft template [42]. However, development of simple and template-free methods for the synthesis of nanostructured cobalt oxides that present superior electrochemical behaviors has received continuous interest.

In this work, nanoflakes of cobaltous oxide using a simple template-free electrodeposition procedure was synthesized and characterized.

---

[*] Corresponding author. Tel.: +98 728 46 92 114; fax: +98 728 46 92 111.
E-mail address: hheli7@yahoo.com (H. Heli).

0013-4686/$ – see front matter © 2009 Elsevier Ltd. All rights reserved.
doi:10.1016/j.electacta.2009.11.047

2. Experimental

2.1. Chemicals and reagents

All chemicals used in this work including $Co(NO_3)_2{\cdot}6H_2O$ were of analytical grade from Merck and used as received. All solutions were prepared by doubly distilled water.

2.2. Apparatus

Electrochemical measurements were carried out in a conventional three-electrode cell contained 100 mM NaOH solution as supporting electrolyte which powered by an electrochemical system comprising of AUTOLAB system with PGSTAT30 and FRA2 boards (Eco Chemie, Utrecht, The Netherlands). CV data were recorded in the analogue mode with a fast analogue scan generator (SCANGEN) in combination with a fast AD converter (ADC 750). The system was run on a PC using GPES and FRA 4.9 softwares. For impedance measurements, the frequency range of 100 kHz to 25 mHz was employed. The ac voltage amplitude used was 10 mV and the equilibrium time was 5 s. A dual Ag/AgCl-Sat'd KCl (from Metrohm) [+197 mV vs. SHE] and a platinum disk were used as reference and counter electrodes, respectively. The working electrode was a platinum (Pt) electrode (modified with cobaltous oxide or else, from Azar Electrode Co., Iran) exposing surface area of 0.0314 cm^2.

Microstructure of the electrodeposited oxide was studied using different surface microscopy techniques. Scanning electron microscopy (SEM) was performed by a Tescan Vega II HiVac instrument, equipped with the energy dispersive X-ray elemental analysis capabilities (EDX) to measure the chemical composition of the upper most layers of the electrode surface. Atomic force microscopy (AFM) was performed in ambient conditions using Nanosurf Mobile S instrument, operating in non-contact mode. Scanning tunneling microscopy (STM) was done *ex situ* at ambient temperature in air in constant current mode using NAMA-STM instrument model SS2. Typical tunneling current and applied voltages for STM imaging were 0.5 nA and 1–2 V, at scan rate of 2 Hz.

XRD (X-ray diffraction) patterns were measured by a Philips X'Pert, The Netherlands, using Cu $K\alpha$ radiation at 40 kV and 30 mA in the 2θ degree range from 10° to 90°.

2.3. Preparation of the nanoflakes of cobaltous oxide electrode

Prior to each electrode modification, traces of cobalt species were removed from the Pt surface by soaking the electrode in nitric acid (50%, v/v) for a few minutes. Successively, the electrode was polished with 0.05 μm alumina suspension on a piece of chamois leather, followed by sonication for 5 min in an ultrasonic bath in a 1:1 ethanol/redistilled water mixture. The electrode was then transferred to the 1.0 M sulfuric acid solution. Potential in the range of −250 to 1750 mV in a regime of cyclic voltammetry was applied for 20 cycles. Afterward, the electrode was rinsed thoroughly with distilled water and placed to the cell. Films of cobaltous hydroxide ($Co(OH)_2$) were first electrodeposited on the Pt surface potentiostatically from a 100 mM cobalt nitrate (II) solution at −1000 mV for 15 s. The high negative potential applied to the working electrode causes the electrolyte (water) to be decomposed into hydrogen gas and the medium near the electrode to be locally alkaline. Subsequently, the cobalt (II) ions precipitate as cobalt (II) hydroxide. Then the electrode was thoroughly washed with doubly distilled water and dried in air at room temperature to obtain a CoO coating for XRD and surface morphology investigations in air, and then, transferred to the working cell as the working electrode for the electrochemical investigations. The Pt electrode surface covered with nanoflakes of cobaltous oxide is denoted as nano-CoO throughout the text. All studies were carried out at room temperature.

3. Results and discussion

3.1. XRD

Fig. 1 shows a typical X-ray diffraction pattern of as synthesized nanoflakes of the cobaltous oxide sample. Nanoflakes of the cobaltous oxide were randomly oriented polycrystalline with main diffraction peaks at the 2θ values of 11°, 23°, 34°, 35°, 39°, 46°, 60° and 61°, correspond to (0 0 3), (0 0 6), (1 0 0), (1 0 2), (1 0 5), (1 0 8), (1 1 0) and (1 1 3) reflections, respectively [43].

3.2. Surface morphology

In order to investigate the surface morphology and the structure of the electrodeposited cobaltous oxide, different microscopy methods were employed. Fig. 2 shows the scanning electron micrographs of the bare Pt electrode surface (A) and nano-CoO electrode surface with two different magnifications (B and C). The Pt electrode surface has a smooth morphology, while relatively uniform nanoflakes of cobaltous oxide are packed on the Pt surface. Tenuous flakes growing on the entire surface consisting shaggy vertical leaves are clearly seen in this figure. The dimensions of these flakes can attain 800 nm, while they have an average thickness of around 20 nm. Fig. 3 shows EDX spectra of as deposited nanoflakes. Cobalt and oxygen were the main detected elements and platinum was also found as the substrate of the deposit. This indicates that the Pt substrate was covered with the cobaltous oxide layer. It is difficult to determine the Co/O ratio of the nanoflakes, because as a lighter element, the intensity of the EDX detection for oxygen is uncertain.

In order to obtain further details of the surface structure, such as thickness and roughness, AFM was used. Fig. 4 shows an AFM topology of the surface of nano-CoO electrode corresponds to 2D (A) and 3D (B) images recorded over an area of 1000 nm × 1000 nm. The 2D image of nano-CoO electrode surface consists of flakes growing on the entire surface. The existence of <30-nm thick sheet in the cobaltous oxide film is clearly obvious in 3D AFM image which is characterized by nearly knoll type projection in the *z*-direction. In addition, a parameter commonly used to quantitatively characterize surface films is the surface roughness which can be represented by the root-mean-square roughness (standard deviation of the surface height within the given area). This parameter can be determined from AFM images. The root-mean-square roughness for the cobaltous oxide film is obtained as 35.7 nm.

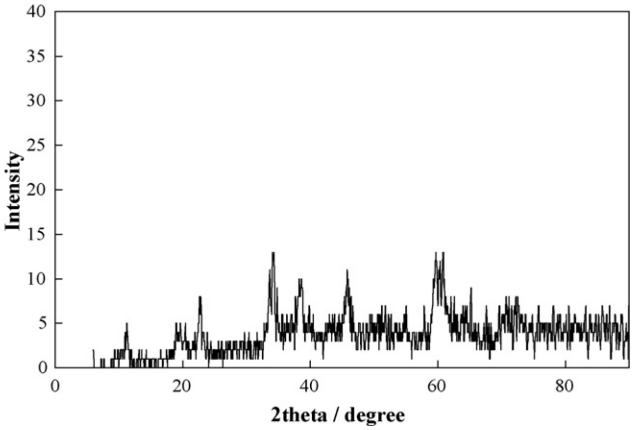

Fig. 1. Typical X-ray diffraction pattern of as synthesized nanoflakes of the cobaltous oxide sample.

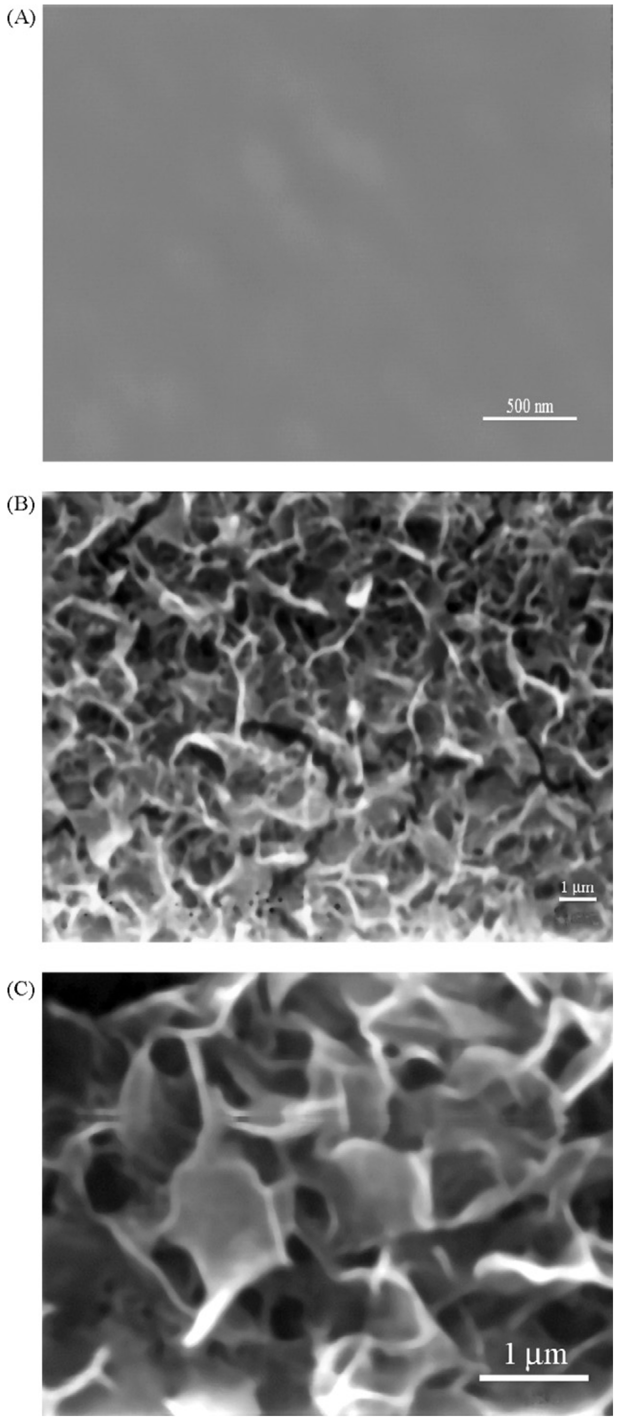

Fig. 2. SEM micrographs of the bare Pt electrode (A) and nanoflakes of cobaltous oxide with two magnifications (B and C).

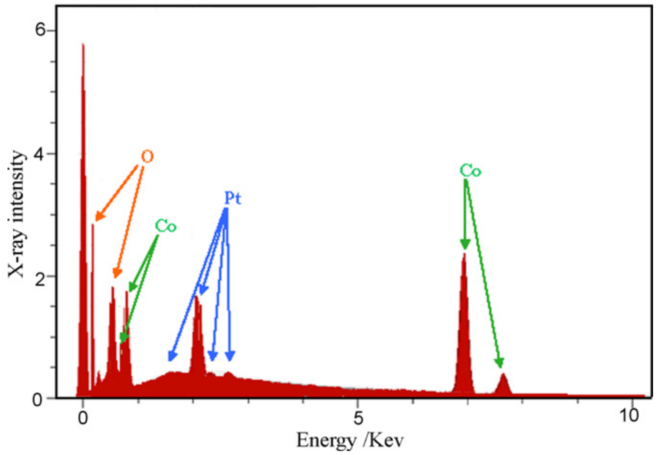

Fig. 3. EDX spectra of the nanoflakes of cobaltous oxide.

STM technique is a powerful tool to analyze surface characteristics of thin films grown electrochemically. This technique has higher imaging resolution than AFM, and it will favor the finer features of flake structure. An STM topology of nano-CoO electrode surface recorded over an area of 4242 nm × 3850 nm is depicted in Fig. 5. Vertical sheets of cobaltous oxide film are obviously seen in the 2D image of the electrode surface (Fig. 5A). The 3D image shows that these sheets have an average height of about 100 nm, the length of a few hundreds nanometer and a thickness of around 30 nm (Fig. 5B). The mean distance between two neighbor sheets is about 50 nm. This morphology exposes maximum surface area that is proper for catalytic purposes and can increase the current efficiency.

3.3. Cyclic voltammetry

Typical cyclic voltammogram of nano-CoO electrode, transferred to a 100 mM NaOH solution recorded in the range of −250 to 700 mV at a potential sweep rate of 50 mV s^{-1} is shown in Fig. 6, main panel. During the potential sweep in positive direction, two oxidation peaks at about 350 mV (I′a) and 620 mV (IIa)

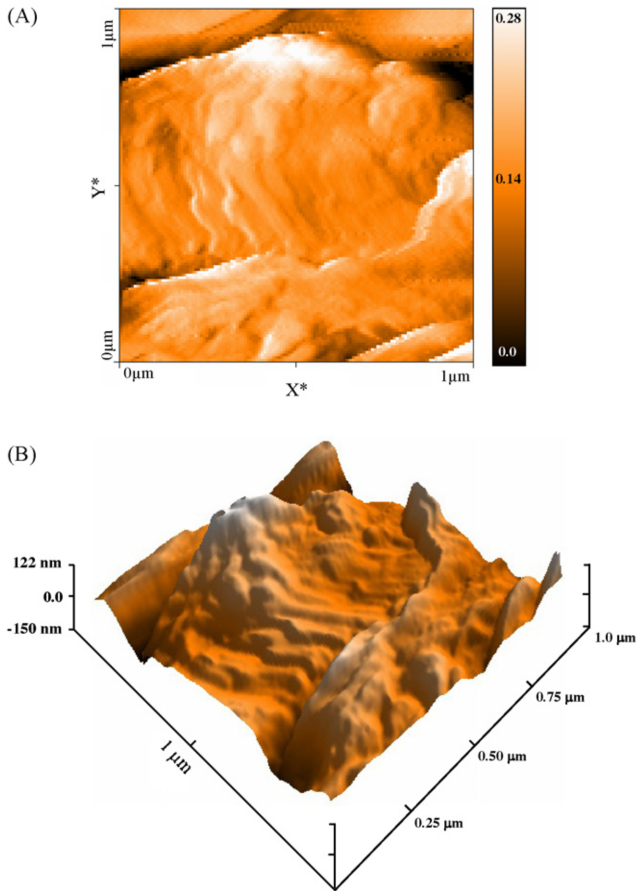

Fig. 4. 2D (A) and 3D (B) AFM images of the deposited nanoflakes of cobaltous oxide on the Pt electrode surface.

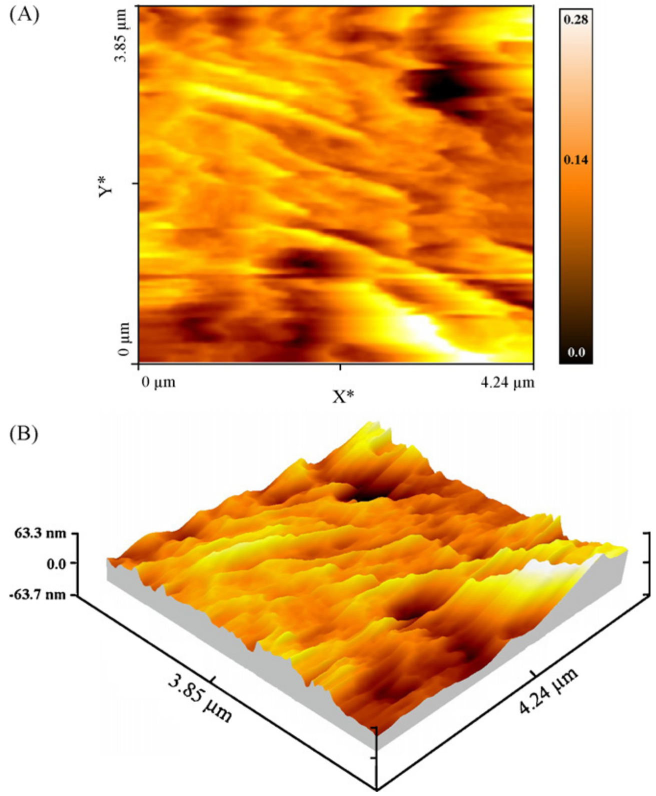

Fig. 5. 2D (A) and 3D (B) STM images of the deposited nanoflakes of cobaltous oxide on the Pt electrode surface.

were observed. The cathodic peaks at 113 mV (Ic) and 520 mV (IIc) correspond to the reduction of the various cobalt oxide species formed during the positive sweep. One further point observed in the voltammogram shown in this figure is that peak I′a is sharper and the corresponding charge is 18% higher, compared to peak Ic. Preliminary, this peak may contain two strongly overlapped peaks. Fig. 6, inset A, shows the derivative voltammogram (time derivative of current *vs.* potential) of the voltammogram represented in the main panel. As observed, the derivative voltammogram contained a broad peak located at potential of peak I′a. This indicates that peak I′a is really comprised two overlapped anodic peaks (denoted as Ia1 and Ia at lower and higher potentials, respectively). Appearance of three anodic peaks in the voltammogram for cobalt oxide-based electrodes has been reported previously [12,19–21,24,34]. The electrochemical behavior of the cobalt oxides is relatively complex and several oxidation states included in different cobalt oxide species, such as spinel Co(II,III) oxide (Co_3O_4), cobaltous oxide (CoO), cobaltic oxide (Co_2O_3), cobalt oxyhydroxide (CoOOH), cobalt dioxide (CoO_2) with various crystallographic forms [19–21], are formed during potential sweep. In addition, physical and chemical status of the electrodeposited cobalt species are strongly affected by hydration effects due to their impact on the Gibbs energy values of the redox transitions [20]. However, there is not a consistency in the literature on the entity of peak Ia1: some authors have related it to the adsorptive oxidation process of oxygen containing species of water/hydroxide ions on the cobalt oxide surface [12,21] according to the following equations:

$$\mathrm{OH^- \rightarrow OH_{ads} + e^-} \tag{1}$$

$$\mathrm{H_2O \rightarrow OH_{ads} + H^+ + e^-} \tag{2}$$

while for some authors, this peak was found as a single anodic peak [19], or accompanied with a cathodic counterpart [20,34]. In both later cases, this peak located before the transition Ia/Ic and it has been related to the oxidation of Co(II) species according to the following equation:

$$\mathrm{3Co(OH)_2 + 2OH^- \rightarrow Co_3O_4 + 2e^- + 4H_2O} \tag{3}$$

Anyway, peak Ia1 appeared in the voltammograms as a well-defined peak in some cases [19–21,34], did not appeared in some others [44], and here, it strongly overlapped with peak Ia and it seems that the interpretation of adsorbing oxygen containing species for this peak is more reliable. It seems that the appearance and the redox potential of this peak strongly depend on the composition of electrodeposition solution, electrodeposition route and the sweeping potential rang.

The redox transitions I and II have formal potentials of 170 and 500 mV which derived from cyclic voltammograms recorded at low

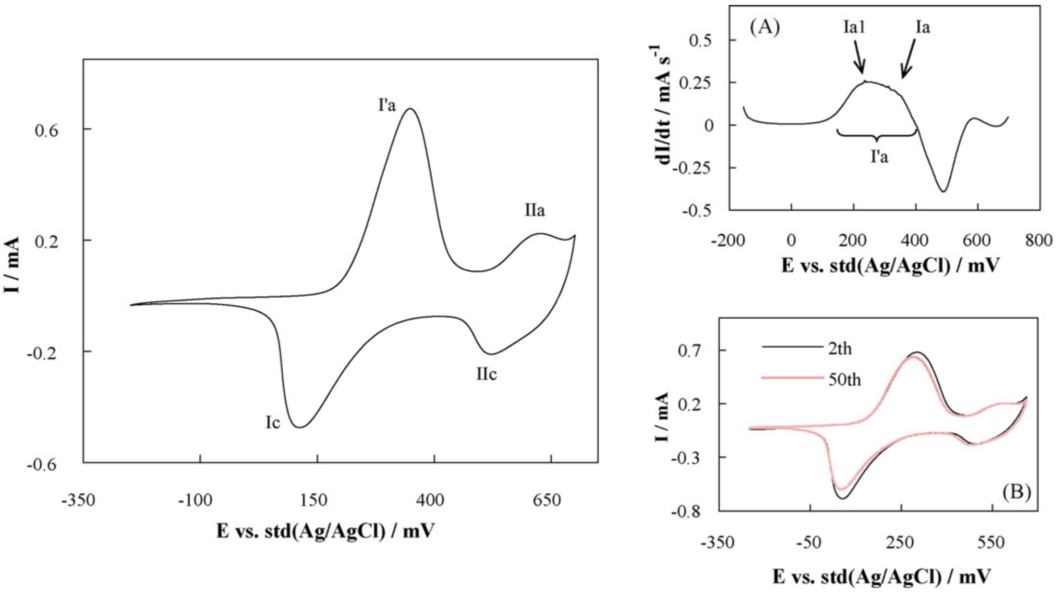

Fig. 6. Typical cyclic voltammogram of nano-CoO electrode in 100 mM NaOH solution in the range of −250 to 700 mV recorded at a potential sweep rate of 50 mV s^{-1}. *Inset A*: The derivative voltammogram (time derivative of current *vs.* potential) of the voltammogram represented in the main panel. *Inset B*: The second and 50th cyclic voltammograms of nano-CoO electrode in 100 mM NaOH solution at a potential sweep rate of 50 mV s^{-1}.

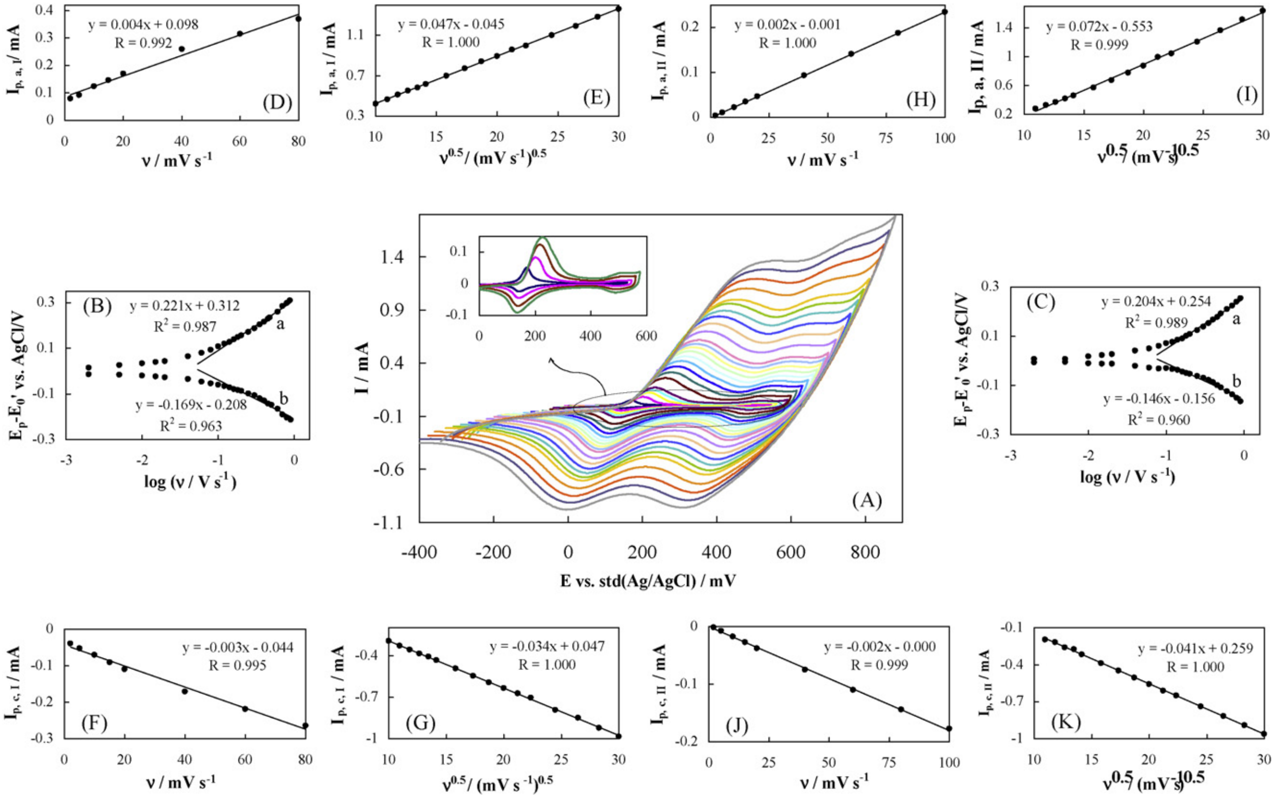

Fig. 7. (A) Cyclic voltammograms of nano-CoO electrode in 100 mM NaOH solution. Potential sweep rates from inner to outer are: 2, 5, 10, 15, 20, 40, 60, 80, 100, 120, 140, 160, 180, 200, 250, 300, 350, 400, 450, 500, 600, 700, 800, and 900 mV s^{-1}. (B and C) Plot of E_p vs. log ν for cyclic voltammograms depicted in A panel for anodic peaks (a) and cathodic peaks (b) for Co(II)/Co(III) (B) and Co(III)/Co(IV) (C) transitions. (D–G) The dependency of anodic (D and E) and cathodic (F and G) peak currents on the potential sweep rate at lower values of 2–80 mV s^{-1} (D and F) and on the square roots of sweep rate at higher values of 100–900 mV s^{-1} (E and G) for Co(II)/Co(III) transition. (H–K) The dependency of anodic (H and I) and cathodic (J and K) peak currents on the potential sweep rate at lower values of 2–100 mV s^{-1} (H and J) and on the square roots of sweep rate at higher values of 120–900 mV s^{-1} (I and K) for Co(III)/Co(IV) transition.

potential sweep rates (vide infra). They can be attributed to the Co(II)/Co(III) (Ia/Ic) and Co(III)/Co(IV) (IIc/IIa) redox transitions in solid state of cobaltous oxide crystal, respectively. The solid-state redox reactions occurring in transitions I and II can be represented as follows [19–21]:

$$Co_3O_4 + OH^- + H_2O \rightarrow 3CoOOH + e^- \quad (4)$$

$$CoOOH + OH^- \rightarrow CoO_2 + H_2O + e^- \quad (5)$$

Inset B in Fig. 6 shows the second and 50th cyclic voltammograms of nano-CoO electrode in a 100 mM NaOH solution. As observed, the peak current related to the Co(II)/Co(III) transition in 50th cycle decreases slightly (5.5%) and the peak potential shifts to negative values about 3% upon potential sweeping, while the current and potential of the Co(III)/Co(IV) transition show no considerable changes. This indicates that the nanoflakes of cobaltous oxide offer very good electrochemical stability in the solution.

Cyclic voltammograms of nano-CoO electrode in 100 mM NaOH solution recorded at different potential sweep rates in a wide range of 2–900 mV s^{-1} are shown in Fig. 7A. Well-defined peaks with mid-peak potential of 170 and 500 mV appear in the voltammograms and the peak-to-peak potential separation (at the potential sweep rate of 5 mV s^{-1}) is 59 and 24 mV for Co(II)/Co(III) and Co(III)/Co(IV) redox transitions, respectively. The peak-to-peak potential separations deviated from the theoretical value of zero and increases at higher potential sweep rates. This indicates a limitation in the charge-transfer kinetics arising from the chemical interaction between the electrolyte ions and the modifier film, the lateral interaction of the immobilized redox couples present on the surfaces, dominated by electrostatic factors, coupled diffusion-migration processes in the bulk of film and/or the presence of non-equivalent sites in the film. In addition, the average value of full width at half height for peak Ia is ≈66 mV. This value is lower than the theoretical value for noninteracting, one-electron surface sites of 90 mV [45]. This was attributed to attractive site–site interactions [46–48]. On the other hand, for peak IIa, this value is ≈126 mV which is higher than 90 mV. Therefore, repulsive site–site interactions dominated for transition II.

The kinetics of charge transfer across the cobaltous oxide film, which is accompanied with ion penetration across the film/solution interface, can be investigated by cyclic voltammograms represented in Fig. 7A. Laviron derived a general expression for the linear potential sweep voltammetric response in the case of surface-confined electroreactive species at small concentration [49]. The expression for peak-to-peak separation (ΔE_p) > 200/n mV where n is the number of exchanged electrons, is as follows:

$$E_{p,a} = E^{0'} + X \ln\left[\frac{1-\alpha_s}{m}\right] \quad (6)$$

$$E_{p,c} = E^{0'} + Y \ln\left[\frac{\alpha_s}{m}\right] \quad (7)$$

$$\ln k_s = \alpha_s \ln(1-\alpha_s) + (1-\alpha_s)\ln\alpha_s - \ln\left(\frac{RT}{nF\nu}\right) - \alpha_s(1-\alpha_s)\frac{nF\,\Delta E_p}{RT} \quad (8)$$

where $X = RT/(1-\alpha_s)nF$, $Y = RT/\alpha_s nF$, $m = (RT/F)(k_s/n\nu)$, $E_{p,a}$ and $E_{p,c}$ are the anodic and cathodic peak potentials, respectively, and α_s, k_s and ν are the electron-transfer coefficient, apparent charge-transfer rate constant and potential sweep rate, respectively. From

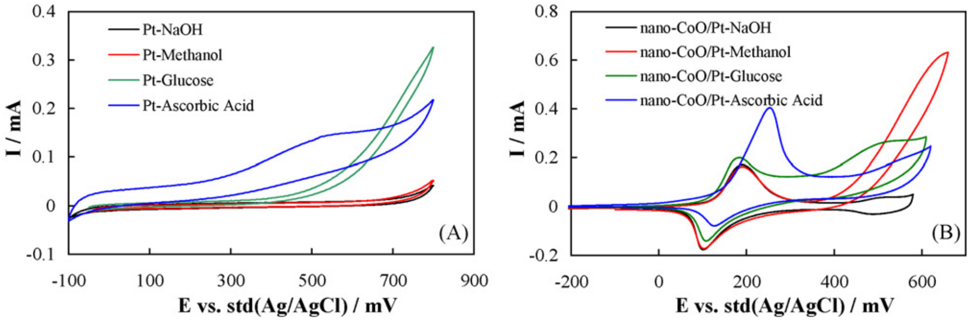

Fig. 8. (A) Cyclic voltammograms of the bare Pt electrode in 100 mM NaOH solution in the absence and presence of 5 mM ascorbic acid, glucose and methanol. The potential sweep rate was 50 mV s^{-1}. (B) Cyclic voltammograms of nano-CoO electrode in 100 mM NaOH solution in the absence and presence of 5 mM ascorbic acid, glucose and methanol. The potential sweep rate was 50 mV s^{-1}.

these expressions, α_s can be determined by measuring the variation of the peak potential with respect to the potential sweep rate, and k_s can be determined for electron transfer between the electrode and the surface deposited layer by measuring the ΔE_p values. Fig. 7B and C shows the plot of $(E_{p,a} - E^{0'})$ with respect to the logarithm ν for transition I and II, respectively. It can be observed that for potential sweep rates >100 mV s^{-1}, the values of $(E_p - E^{0'})$ are proportional to the logarithm of the potential sweep rate indicated by Laviron. Using the plots and Eqs. (6)–(8), the value of α_s was obtained as 0.31 for Co(II)/Co(III) transition and 0.35 for Co(III)/Co(IV) transition. In addition, the mean values of k_s were obtained as 0.6 and 0.99 s^{-1} for Co(II)/Co(III) and Co(III)/Co(IV) redox transitions, respectively. These values are higher than that reported for the cobaltous oxide nanoparticles [24], reflecting a higher reactivity for the cobalt species with nanoflake shape. All these kinetics parameters have also summarized in Table 1.

The anodic and cathodic currents for both Co(II)/Co(III) and Co(III)/Co(IV) transitions in voltammograms represented in Fig. 7A are proportional to the potential sweep rate at low values of 2–80 mV s^{-1} (Fig. 7D and F) for Co(II)/Co(III) transition and 2–100 mV s^{-1} (Fig. 7H and J) for transition Co(III)/Co(IV). These results are attributed to the electrochemical activity of immobilized redox couples at the electrode surface. From the slope of the lines and using the equation [50]:

$$I_p = \left(\frac{n^2F^2}{4RT}\right)\nu A\Gamma^* \qquad (9)$$

where A is the electrode surface area, Γ^* is the surface coverage of the redox species and I_p is the peak current, and also taking the average of both cathodic and anodic currents, the total surface coverage of the electrode with the modifier film of cobalt was derived as 1.05×10^{-7} mol cm^{-2} for Co(II)/Co(III) transition and 7.04×10^{-8} mol cm^{-2} for Co(III)/Co(IV) transition. These values are also reported in Table 1. It should be expressed that the values of Γ^*s are different for two transitions: it may be due to limitation in conversion of redox species to each other and/or resistance to transformation of interlayer species to the other ones.

In the high range of potential sweep rates of 100–900 mV s^{-1} (Fig. 7E and G) for Co(II)/Co(III) transition and 120–900 mV s^{-1} (Fig. 7I and K) for transition Co(III)/Co(IV), the peak current–potential sweep rate dependencies are of square root forms, signifying the dominance of diffusion processes as the rate limiting steps in the total redox transitions of the modifier film. These diffusion processes which also occurs during the redox processes of other transition metal oxides [24,51–55], may be due to the charge neutralization and ion exchange between two ionic conductors of modifier film and the adjacent solution.

Table 1
The electron-transfer coefficient and apparent charge-transfer rate constant of various redox transitions cobalt film obtained from cyclic voltammograms recorded at different potential sweep rates.

Redox transition	α_s	k_s/s^{-1}	$\Gamma^* \times 10^8/\text{mol cm}^{-2}$	Reference
Co(II)/Co(III)	0.31	0.60	10.5	This work
Co(III)/Co(IV)	0.3	0.22	0.336	[7]
Co(III)/Co(IV)	0.35	0.99	7.04	This work

In order to inspection the electrocatalytic reactivity of the nanoflakes, electrooxidation of ascorbic acid, glucose and methanol as model compounds was investigated on nano-CoO electrode surface using cyclic voltammetry. Fig. 8A shows cyclic voltammograms of 5 mM ascorbic acid, glucose and methanol in the running electrolyte using a bare Pt electrode. In the voltammograms, methanol and glucose represent weak oxidation signals; no well-defined anodic peak appeared in the voltammograms. Ascorbic acid is oxidized on the bare Pt surface and represents an anodic peak with a peak potential of ≈550 mV. Fig. 8B shows cyclic voltammograms of 5 mM ascorbic acid, glucose and methanol in the running electrolyte using nano-CoO electrode. In these voltammograms, in the presence of ascorbic acid and glucose, the anodic currents of both Co(II)/Co(III) and Co(III)/Co(IV) transitions and also the associated anodic charges increased dramatically. Subsequently, the cathodic currents and the corresponding charges of these transitions decreased. Therefore, ascorbic acid and glucose are oxidized on the surface of nano-CoO electrode via a surface mediation electron transfer in two steps by two active catalysts of Co(III) and Co(IV) moieties. Moreover, these compounds are oxidized on the nano-CoO electrode surface at very lower potentials with respect to the bare Pt electrode. In the case of the methanol, however, only the anodic current of Co(III)/Co(IV) transition is increased following by a decrease in the corresponding cathodic current. While, the anodic and cathodic currents of Co(II)/Co(III) transition remain unchanged. Therefore, methanol is oxidized only by active catalyst of Co(IV) moiety which is generated at more positive potentials. These results indicate that these model compounds are oxidized on the nano-CoO electrode surface in an electrocatalytic manner. The electrocatalytic oxidations of ascorbic acid and glucose can be represented as:

$$\text{Red} \rightarrow \text{Ox1} + e^- \qquad (10\text{-}1)$$

followed by:

$$\text{Ox1} \rightarrow \text{Ox2} + e^- \qquad (10\text{-}2)$$

being the sum of:

$$\text{Co(II)} \rightarrow \text{Co(III)} + e^- \qquad (11\text{-}1)$$

$$\text{Red} + \text{Co(III)} \rightarrow \text{Ox1} + \text{Co(II)} \qquad (12\text{-}1)$$

and

$$\mathrm{Co(III)} \rightarrow \mathrm{Co(IV)} + \mathrm{e}^{-} \tag{11-2}$$

$$\mathrm{Red/Ox1} + \mathrm{Co(IV)} \rightarrow \mathrm{Ox1/Ox2} + \mathrm{Co(III)} \tag{12-2}$$

and methanol being oxidized as:

$$\mathrm{Co(III)} \rightarrow \mathrm{Co(IV)} + \mathrm{e}^{-} \tag{11-2}$$

$$\mathrm{Red} + \mathrm{Co(IV)} \rightarrow \mathrm{Ox} + \mathrm{Co(III)} \tag{12-3}$$

The electrocatalytic oxidation of these model compounds confirms the applicability of the stable cobaltous oxide electrode toward the oxidation of different classes of electroreactive compounds and makes it proper for the miniaturized sensing devices.

3.4. Electrochemical impedance spectroscopy

Electrochemical impedance spectroscopy can access relaxation phenomena over many orders of magnitude and has been employed for the study of the kinetics of the charge-transfer process into and across the electroreactive films [51–54,56,57].

The processes occurred in the course of redox transition of metal oxide are a combination of electron transfer at the oxide/solution interface, slow diffusion of interstitial ions in the solid lattice of metal oxide, flipping-flopping of ion across the oxide/solution interface and fast ion transport in the bulk of solution [39,46,48,56,58,59]. Accordingly, the Faradaic current which passes through the cobaltous oxide/solution interface is a function of hydroxide ion concentration and the potential at this interface and two potential steps of δE_1: through the bulk of oxide and δE_2: at the cobaltous oxide/solution interface dominate. Therefore, the Faradaic impedance is:

$$Z_f = \frac{\delta E_1}{\delta I_f} + \frac{\delta E_2}{\delta I_f} \tag{13}$$

and the flux of charged species at the cobaltous oxide/solution interface (using the Taylor's series expansion and Laplace transformation) is [59]:

$$\frac{\delta J_{ion}}{\delta E_2} = \frac{\xi_{ion}}{1 + \varsigma_{ion}[\coth[d(j_{\omega}/D_{ion})^{0.5}]/(j\omega D_{ion})^{0.5}]} \tag{14}$$

In this equation:

$$\xi_{ion} = b^{1}_{ion}\, k^{1}_{ion}\, (C_{ion} - C_{ion,min}) - C_{ion,soln} b^{-1}_{ion} k^{-1}_{ion} (C_{ion,max} - C_{ion}) \tag{15}$$

$$\varsigma_{ion} = k^{1}_{ion}\ \exp[b^{1}_{ion}(E - E^{0})] + k^{-1}_{ion}\ \exp[b^{-1}_{ion}(E - E^{0})]C_{ion,soln} \tag{16}$$

where the subscript ion represents the solid-state diffusing ion. d is the mean diffusion length (equals to the thickness of the nanoflakes of cobaltous oxide), D_{ion} is the diffusion coefficient of hydroxide ion through the oxide, ω is the angular frequency of ac the imposed sinusoidal signal, $j = \sqrt{-1}$ and E^0 is the formal potential. Also, $C_{ion,min}$ and $C_{ion,max}$ are minimum and maximum concentration sites available for insertion of hydroxide ion in the oxide structure, respectively, $C_{ion,soln}$ is the ion concentration in the bulk of solution, and C_{ion} is the concentration of occupied sites in the oxide. In these equations, ξ is negative/positive for the insertion/deinsertion of hydroxide ion.

Nanoflakes of cobaltous oxide have very small thickness and therefore, δE_1 is negligible in comparison with δE_2. So, the equation of Faradaic impedance (Eq. (13)) is reduced to:

$$Z_f = \frac{\delta E_2}{\delta I_f} = \frac{1}{F\xi_{ion}} \left\{ \frac{1 + (\varsigma_{ion}\tau_{ion} \coth(j\omega\tau_{ion})^{0.5})}{d(j\omega\tau_{ion})^{0.5}} \right\} \tag{17}$$

where $\tau_{ion} = d^2/D_{ion}$ is the time constant of the diffusion process.

One another approach which can be used to interpret the impedance response is the model of the wave transmission in a finite-length RC transmission line [56] which was used for a porous electrode or an electroreactive film [60]. In this expression, the Faradaic impedance is:

$$Z_f = R_{ct} + Z_{FLW} = R_{ct} + R_{FLW} \left\{ \mathrm{ctnh} \left(\frac{(j\omega R_{FLW} C_{FLW})^{0.5}}{(j\omega R_{FLW} C_{FLW})^{0.5}} \right) \right\} \tag{18}$$

where R_{ct} is the charge-transfer resistance, R_{FLW} analogizes the resistance of the diffusion of a species through a finite length and C_{FLW} describes the capacitance of the finite space. By comparing Eqs. (17) and (18), it can be deduced that:

$$\tau_{ion} = R_{FLW}C_{FLW} = \frac{d}{D_{ion}}^{2} \tag{19}$$

$$\frac{d}{\varsigma_{ion}\tau_{ion}} = \frac{R_{ct}}{R_{FLW}} \tag{20}$$

$$\xi_{ion} = \frac{1}{FR_{ct}} \tag{21}$$

Nyquist diagrams using nano-CoO electrode in 100 mM NaOH solution in a wide range of dc-potential were recorded. As the bias of the system is systematically varied, different signatures were observed in the Nyquist diagrams and different processes dominated the electrochemical characteristics of the film. These behaviors were modeled by the dominance of different components in electrical equivalent circuits (vide infra). The Nyquist diagrams will be better interpreted if constant phase elements (CPEs) were replaced with the pure capacitances for the capacitive semicircle which the centers were deviated from real impedance axis. The impedance of this element is [61]:

$$Z_{CPE} = \frac{1}{T_0(j\omega)^{n}} \tag{22}$$

which T_0 is constant phase element coefficient and n is constant phase element exponent. n is equal to unity for perfect capacitance.

In the Nyquist diagram recorded at the dc-potential of 110 mV (Fig. 9A), two capacitive depressed semicircles appeared (indicated by arrows). The dc-potential of 110 mV is around the onset potential of anodic peak Ia. At this potential, the reactions occurred in the course of peak Ia being to start (reactions (1), (2) and (4)). The high-frequency semicircle can be attributed to the Co(II)/Co(III) transition and the low-frequency one to the adsorption reaction of oxygen containing species. This sequence of relation is due to the corresponding higher time constant for adsorption processes at the electrode surfaces, compared to the adsorbed-free redox transitions [62]. The adsorption processes usually represent capacitive semicircle which appear at lower frequencies in the Nyquist diagrams [62]. Another point in this Nyquist diagram is that the diameter of high-frequency semicircle is relatively low, which indicates that the rate of redox transition of Co(II)/Co(III) is very high. This fact which was also confirmed by cyclic voltammetry (vide supra and see Table 1), is due to the high reactivity of special nanoflake structure. An electrical equivalent circuit model was employed for the analysis of this Nyquist diagram which is shown in the inset of Fig. 9A and the fitted Nyquist diagram using this equivalent circuit is also shown. In this circuit, R_s, $\mathrm{CPE_{dl}}$, R_{ct}, $\mathrm{CPE_{ads}}$ and R_{ads} are the solution resistance, a constant phase element describes the double layer capacitance, charge-transfer process of Co(II)/Co(III) redox couple and constant phase and resistance elements describe the low frequencies adsorption response.

At dc-potential of 140 mV (Fig. 9B), the diameter of the low-frequency semicircle is lowered. This is due to the potential dependency of the adsorption process of oxygen containing species

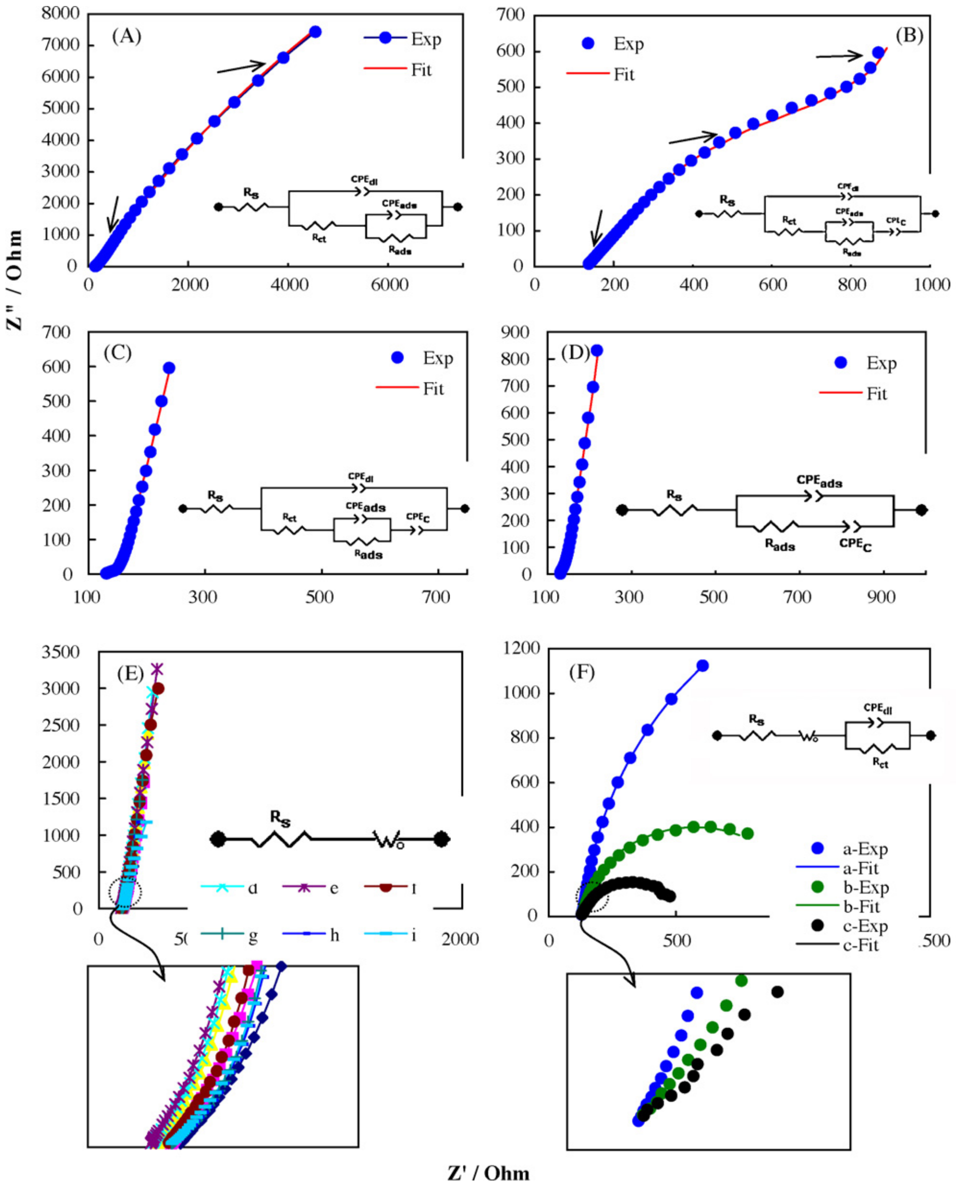

Fig. 9. Nyquist diagrams recorded for nano-CoO electrode in 100 mM NaOH solution and the corresponding electrical equivalent circuits at various dc-offset potentials: (A) 110 mV, (B) 140 mV, (C) 180 mV, (D) 210 mV, (E) a, 250 mV; b, 290 mV; c, 320 mV; d, 360 mV; e, 390 mV; f, 430 mV; g, 470 mV; h, 500 mV; i, 540 mV, and (F) a, 570 mV; b, 610 mV; c, 650 mV.

at the cobaltous oxide surface. Also, one additional signature is being to start at very low frequencies. At dc-potential of 180 mV (Fig. 9C), similar pattern to that observed at 140 mV is observed, otherwise that the diameter of semicircles are so decreased and the very low-frequency response is revealed to be a capacitive response. This near vertical line at low frequency is related to the well-known redox capacitance behavior of cobalt oxides [63]. The electrical equivalent circuit compatible with the Nyquist diagrams shown in Fig. 9B and C and the fitted Nyquist diagrams using this equivalent circuit are represented. In this circuit, R_s, CPE_{dl} and R_{ct} are the solution resistance, a constant phase element describes the double layer capacitance, charge-transfer process of Co(II)/Co(III) redox couple. Also, CPE_{ads} and R_{ads} are constant phase and resistance elements describe the adsorption process and CPE_C describes the low-frequency linear tail.

The dc-potential of 210 mV is so positive that causes the redox transition Co(II)/Co(III) to be occur with a high rate and the capacitive semicircle related to this process is eliminated from the Nyquist diagram recorded at this dc-potential (Fig. 9D). In Fig. 9D, the adsorption process (reactions (1) and (2)) is continued to be occur faster and faster; a small semicircle related to this process is flowed by the vertical line response. Nyquist diagram recorded at this dc-potential can be modeled by the electrical equivalent circuit shown in the inset. In this circuit, R_s, CPE_{ads} and R_{ads} are the solution resistance and constant phase and resistance elements describe the adsorption process and CPE_C describes the low-frequency capacitive response.

In a wide dc-potential range of 250–540 mV, two linear parts observed in the Nyquist diagrams (Fig. 9E). A high-frequency linear response with a slope of ≈4 is followed by a near vertical line at low frequencies. Therefore, it can be related to a coupled process of mass transport by diffusion and charge accumulation in the film. The mass transport process can be an ion exchange process which is occurred to guarantee the charge neutrality of the film and it has been reported that the entity of diffusing species in the bulk of redox transitions is the hydroxide ion [19]. The signature of impedance response in this figure is a typical behavior of supercapacitances [63] which is a characteristic of coupled diffusion-accumulation

Table 2
Values of the equivalent circuit elements obtained by fitting the experimental results in the Nyquist diagrams represented in Fig. 9E, the corresponding relative errors, values of the diffusion coefficient of hydroxide ion and the electrode capacitance at each bias.

Bias/mV	R_s/Ω	$W_o - R\,(R_{FLW})/\Omega$	$W_o - \tau/s$	$W - n$	$D_{ion} \times 10^{11}/cm^2\,s^{-1}$	$W_o - C\,(C_{FLW})/mF$
250	121.3 (0.52%)	31.39 (8.0%)	0.13 (8.9%)	0.46 (0.24%)	3.08	4.14
290	119.8 (0.5%)	28.17 (8.1%)	0.08 (8.9%)	0.47 (0.19%)	4.95	2.87
320	118.2 (0.51%)	28.4 (7.8%)	0.060 (8.5%)	0.47 (0.16%)	6.63	2.12
360	120.1 (0.52%)	29.34 (7.6%)	0.05 (8.1%)	0.478 (0.15%)	7.92	1.72
390	119.5 (0.46%)	26.13 (7.7%)	0.041 (8.3%)	0.48 (0.14%)	9.85	1.55
430	119.1 (0.48%)	31.41 (6.9%)	0.053 (7.5%)	0.48 (0.15%)	7.47	1.70
470	120 (0.40%)	36.61 (5.6%)	0.11 (6.1%)	0.48 (0.19%)	3.60	3.03
500	119.6 (0.43%)	37.11 (6.0%)	0.17 (6.5%)	0.48 (0.23%)	2.36	4.57
540	120.3 (0.46%)	30.66 (7.3%)	0.13 (8.0%)	0.47 (0.22%)	2.98	4.37

process. The slope of the linear tail at high frequencies is higher than a pure Warburg line (unity) and that in low frequencies is lower than a pure capacitance (infinity). However, based on Eq. (18), the theoretical impedance response should be a line with a slope of unity followed by a vertical line; open circuit terminus Warburg impedance. Therefore, both parts of impedance curves in Fig. 9E are deviated from the ideal ones. This behavior can be explained in terms of anomalous diffusion [64]: higher slope than unity observed for semi-infinite diffusion when the diffusing species wait after each jump for a period drown from a broad power-law distribution. The effect is that some diffusing species stick for a long time in diffusion path and diffusion becomes slower. The electrical equivalent circuit compatible with these Nyquist diagrams and the fitted Nyquist diagrams are shown. In the circuit, R_s and W_o are the solution resistance and the open circuit terminus Warburg element. The values of the electrical element components of this equivalent circuit were obtained by a fitting procedure and reported in Table 2. Using Eq. (18) and the values of the circuit elements, the values of the diffusion coefficient of hydroxide ion in the cobaltous oxide flakes, D_{ion}, were obtained and are reported in Table 2. The diffusion coefficient of hydroxide ion is potential-dependent and changes smoothly and represents a sharp maximum at 390 mV. Similar behavior for the dependency of solid-state diffusion coefficient on the electrode potential has been reported elsewhere [65,66]. At dc-potential of 390 mV, the diffusion coefficient is the highest and the ion movement is occurred with the highest rate. Therefore, the ion accumulation has the minor effect and the capacitance value of the electrode is the lowest (see Table 2).

Another point in the Nyquist diagrams recorded in the dc-potential range of 250–540 mV is that interestingly, no capacitive semicircle is observed related to the Faradaic process of Co(III)/Co(IV) transition. It seems that the rate of this process is too fast to dominate in the impedance response. This is also confirmed by the higher value of apparent charge-transfer rate constant for this redox transition obtained from cyclic voltammetry (see Table 1). Therefore, nanoflakes of cobaltous oxide are potentially a best supercapacitor in the potential range of 250–540 mV which with a negligible resistance represent redox capacitance behavior.

At dc-potential 570–650 mV, the high-frequency linear response is followed by a capacitive semicircle at low frequencies (Fig. 9F). The high-frequency response is related to the response of the electrode material. The low-frequency response is related to the oxygen evolution reaction occurred at this highly positive potential range. Upon increasing dc-potential from 570 to 650 mV, the charge-transfer resistance of the oxygen evolution reaction decreases upon potential becomes more positive. The equivalent circuit shown in the inset was used to interpret the Nyquist diagrams recorded at this potential range. In this circuit, R_s and W are the solution resistance and a Warburg element, while CPE_{dl} and R_{ct} represent a constant phase element describes the double layer capacitance and charge-transfer process of oxygen evolution process.

4. Conclusions

A nanostructured cobaltous oxide film was prepared by electrodeposition on the surface of a Pt electrode without using any hard or soft template. The simplicity and short time of preparation are the main advantages of this synthesis procedure. The kinetic parameters of the redox processes such as electron-transfer coefficients, apparent charge-transfer rate constants and diffusion coefficient were obtained. A careful interpretation of the impedance data obtained at different dc-offset potentials allowed the separation of different processes dominated: charge-transfer processes and mass transport of hydroxide ion via diffusion. The cobaltous oxide nanoflakes represent very fast electron-transfer rate without any suffering from limitation in the charge-transfer processes. They can act as an electron shuttling mediator and represented good electrocatalytic reactivity toward some important compounds due to their unique structure. It can provide potential applications in electrocatalysis and electroanalysis.

Acknowledgment

The financial support of the Research Councils of Islamic Azad University and K.N. Toosi University of Technology and the Iran National Science Foundation (INSF) are gratefully acknowledged.

References

[1] H.S. Nalwa (Ed.), Encyclopedia of Nanoscience and Nanotechnology, American Scientific Publishers, 2004.
[2] T.L. Wade, J.E. Wegrowe, Eur. Phys. J. Appl. Phys. 29 (2005) 3.
[3] C. Brechignac, P. Houdy, M. Lahmani (Eds.), Nanomaterials and Nanochemistry, Springer-Verlag, Berlin Heidelberg, 2007.
[4] H. Weller, Angew. Chem. 35 (1996) 1079.
[5] J.A. Rodriguez, M. Fernandez-Garcia (Eds.), Synthesis, Properties, and Applications of Oxide Nanomaterials, Wiley, NJ, 2007.
[6] C.J. Lin, G.X. Shen, Y.C. Chen, Thin Solid Films 489 (2005) 130.
[7] H. Heli, A. Jabbari, S. Majdi, M. Mahjoub, A.A. Moosavi-Movahedi, S. Sheibani, J. Solid State Electrochem. doi:10.1007/s10008-008r-r0758-1.
[8] H. Heli, A. Jabbari, M. Zarghan, A.A. Moosavi-Movahedi, Sens. Actuators B 140 (2009) 245.
[9] Z.S. Wronski, Int. Mater. Rev. 46 (2001) 1.
[10] E. Hosono, S. Fujihara, I. Honma, M. Ichihara, H. Zhou, J. Power Sources 158 (2006) 779.
[11] E. Barrera, I. Gonzalez, T. Viveros, Solar Energy Mater. Solar Cells 51 (1998) 69.
[12] I.G. Casella, M.R. Guascito, Electrochim. Acta 45 (1999) 1113.
[13] Y. Jyoko, S. Kashiwabara, Y. Hayashi, J. Electrochem. Soc. 144 (1997) L5.
[14] D. Phase, R.J. Choudhary, V. Ganesan, V.R. Reddy, A. Guptaa, N. Selvi, S. Kulkarni, S. Ogale, Solid State Commun. 149 (2009) 277.
[15] L.D. Kadam, S.H. Pawar, P.S. Patil, Mater. Chem. Phys. 68 (2001) 280.
[16] R.N. Thokale, P.S. Patil, M.B. Dongare, Mater. Chem. Phys. 74 (2002) 143.
[17] S. Trasatti, Electrochim. Acta 36 (1991) 225.
[18] L.C. Schumacher, I. Holzhueter, I.R. Hill, M.J. Dignam, Electrochim. Acta 35 (1990) 975.
[19] C. Barbero, G.A. Planes, M.C. Miras, Electrochem. Commun. 3 (2001) 113.
[20] I.G. Casella, M. Gatta, J. Electroanal. Chem. 534 (2002) 31.
[21] I.G. Casella, J. Electroanal. Chem. 520 (2002) 119.
[22] S. Buratti, B. Brunetti, S. Mannino, Talanta 76 (2008) 454.
[23] W. Jia, M. Guo, Z. Zheng, T. Yu, E.G. Rodriguez, Y. Wang, Y. Lei, J. Electroanal. Chem. 625 (2009) 27.

[24] M. Houshmand, A. Jabbari, H. Heli, M. Hajjizadeh, A.A. Moosavi-Movahedi, J. Solid State Electrochem. 12 (2008) 1117.
[25] L.F. Fan, X.Q. Wu, M.D. Guo, Y.T. Gao, Electrochim. Acta 52 (2007) 3654.
[26] C. Xu, Z. Tian, P. Shen, S.P. Jiang, Electrochim. Acta 53 (2008) 2610.
[27] P. Nkeng, J.F. Koening, J.L. Gautier, P. Chartier, G. Poillerat, J. Electrochem. Soc. 402 (1996) 81.
[28] Y. Zhu, H. Li, Y. Koltypin, A. Gedanken, J. Mater. Chem. 12 (2002) 729.
[29] L.C. Schumacher, I.B. Holzhueter, I.R. Hill, K.J. Dignam, Electrochim. Acta 35 (1990) 975.
[30] L.M. Dasilva, J.F.C. Boodts, L.A.D. Faria, Electrochim. Acta 46 (2001) 1369.
[31] S.P. Jiang, A.C.C. Tseung, J. Electrochem. Soc. 137 (1990) 764.
[32] Y. Ni, X. Ge, Z. Zhang, H. Liu, Z. Zho, Q. Ye, Mater. Res. Bull. 36 (2001) 2383.
[33] F. Svegl, B. Orel, I.G. Svegl, C.V. Kaucic, Electrochim. Acta 45 (2000) 4359.
[34] I.G. Casella, M.R. Guascito, J. Electroanal. Chem. 476 (1999) 54.
[35] G. Schmid, Clusters and Colloids, VCH, Weinheim, 1994.
[36] P. Poizot, S. Laruelle, S. Grugeon, L. Dupont, J.M. Tarascon, Nature 407 (2000) 496.
[37] R.L. Penn, A.T. Stone, D.R. Veblen, J. Phys. Chem. B 105 (2001) 4690.
[38] V. Pralong, A. Delahaye-Vidal, B. Beaudoin, J.B. Leriche, J.M. Tarascon, J. Electrochem. Soc. 147 (2000) 1306.
[39] A. Nemudry, P. Rudolf, R. Schollhorn, Chem. Mater. 8 (1996) 2232.
[40] H. Yang, Y. Hu, X. Zhang, G. Qiu, Mater. Lett. 58 (2004) 387.
[41] D. Barreca, C. Massign, S. Daolio, M. Fabrizio, C. Piccirillo, L. Armelao, E. Tondello, Chem. Mater. 13 (2001) 588.
[42] Y. Oaki, H. Imai, J. Mater. Chem. 17 (2007) 316.
[43] L. Markov, K. Petrov, A. Lyubchova, Solid State Ionics 39 (1990) 187.
[44] S. Palmas, F. Ferrara, A. Vacca, M. Mascia, A.M. Polcaro, Electrochim. Acta 53 (2007) 400.
[45] E. Laviron, J. Electroanal. Chem. 122 (1981) 37.
[46] P. Daum, J.R. Lenhard, D. Rolison, R.W. Murray, J. Am. Chem. Soc. 102 (1980) 4649.
[47] M.S. Wrighton, M.C. Palazzotto, A.B. Bocarsly, J.M. Bolts, A.B. Fischer, L. Nadjo, J. Am. Chem. Soc. 100 (1978) 7264.
[48] J.M. Bolts, A.B. Bocarsly, M.C. Palazzotto, E.G. Walton, N.S. Lewis, M.S. Wrighton, J. Am. Chem. Soc. 101 (1979) 1378.
[49] E. Laviron, J. Electroanal. Chem. 101 (1979) 19.
[50] A.J. Bard, L.R. Faulkner, Electrochemical Methods, Wiley, New York, 2001.
[51] S. Majdi, A. Jabbari, H. Heli, A.A. Moosavi-Movahedi, Electrochim. Acta 52 (2007) 4622.
[52] S. Majdi, A. Jabbari, H. Heli, J. Solid State Electrochem. 11 (2007) 601.
[53] M. Hajjizadeh, A. Jabbari, H. Heli, A.A. Moosavi-Movahedi, A. Shafiee, K. Karimian, Anal. Biochem. 373 (2008) 337.
[54] M. Hajjizadeh, A. Jabbari, H. Heli, A.A. Moosavi-Movahedi, S. Haghgoo, Electrochim. Acta 53 (2007) 1766.
[55] S. Motupally, C.C. Streinz, J.W. Weidner, J. Electrochem. Soc. 145 (1998) 29.
[56] E. Barsoukov, J.R. Macdonald, Impedance Spectroscopy, Wiley, NJ, 2005.
[57] H. Heli, M. Hajjizadeh, A. Jabbari, A.A. Moosavi-Movahedi, Biosens. Bioelectron. 24 (2009) 2328.
[58] K. Itaya, T. Ataka, I. Uchida, S. Toshima, J. Am. Chem. Soc. 104 (1982) 4767.
[59] C. Gabrielli, M. Keddam, N. Nadi, H. Perrot, Electrochim. Acta 44 (1999) 2095.
[60] T. Pajkossy, J. Electroanal. Chem. 364 (1994) 111.
[61] R.S. Neves, E.D. Robertis, A. Motheo, J. Electrochim. Acta 51 (2006) 1215.
[62] J.P. Diard, B. Le Gorrec, C. Montella, Cinetique Electrochimique, Hermann, Paris, 1996.
[63] V. Gupta, T. Kusahara, H. Toyama, S. Gupta, N. Miura, Electrochem. Commun. 9 (2007) 2315.
[64] J. Bisquert, A. Compte, J. Electroanal. Chem. 499 (2001) 112.
[65] V.V. Kondratiev, A.V. Tikhomirova, V.V. Malev, Electrochim. Acta 45 (1999) 751.
[66] J.J. Garcia-Jareno, J. Navarro-Laboulais, A. Sanmatias, F. Vicente, Electrochim. Acta 43 (1998) 1045.